Journal of Microscopy, Vol. 223, Pt 3 September 2006, pp. 185–190

Nanoscale scanning transmission electron tomography

P. A. MIDGLEY*, M. WEYLAND*†, T. J. V. YATES*,
I. ARSLAN*, R. E. DUNIN-BORKOWSKI* & J. M. THOMAS*‡
*Department of Materials Science and Metallurgy, University of Cambridge, Pembroke Street, Cambridge CB2 3QZ, U.K.
‡The Royal Institution of Great Britain, 21 Albemarle Street, London W1S 4BS, U.K.

Key words. Electron tomography, nanotechnology, scanning transmission electron microscopy high angle annular dark field (HAADF) imaging.

Summary

Electron tomography enables the study of complex three-dimensional objects with nanometre resolution. In materials science, scanning transmission electron microscopy provides images with minimal coherent diffraction effects and with high atomic number contrast that makes them ideal for electron tomographic reconstruction. In this study, we reviewed the topic of scanning transmission electron microscopy-based tomography and illustrated the power of the technique with a number of examples with critical dimensions at the nanoscale.

Introduction

The potential of nanotechnology will only be fully realized if characterization techniques are available for the study of structures at the nanometre scale. Many proposed nanoscale devices are truly three-dimensional (3D) in their design and high spatial resolution microscopy is required to reveal their full complexity. Transmission electron microscopy (TEM), be it in the form of high-resolution electron microscopy or scanning TEM (STEM), can provide images with extremely high spatial resolution (sub-Å with aberration-corrected instruments) but all TEM images are only two-dimensional projections of a 3D object and as such may be rather misleading. In structural biology, 3D TEM techniques have been developed over many years to study cellular structures (e.g. Marsh *et al.*, 2001). In materials science and engineering, X-ray tomography has been used successfully to reconstruct relatively large 3D structures, such as metallic foams (Banhart, 2001), or to probe the stress in engineering structures (Hirano *et al.*, 1995). At the other end of the resolution scale, the atom probe field ion microscope is able to reconstruct 3D objects with atomic resolution (Miller, 2000) but the sample needs to be conducting and to withstand high field stresses. In contrast, electron tomography allows relatively large structures and devices, from metals to insulators, to be studied (up to ~500 nm in diameter) but with a 3D resolution of ~1 nm allowing the intricate detail of the internal nanostructure to be seen.

Correspondence to: Dr P. A. Midgley. Tel: +44 1223334561; fax: +44 1223334563; e-mail: pam33@cam.ac.uk
†Present address: E13 Clark Hall, Department of Applied and Engineering Physics, Cornell University, Ithaca, NY 14853, U.S.A.

Acquisition and reconstruction

In general, in order to reconstruct a 3D object using an electron tomographic approach, a series of images (projections) must be acquired at angular increments by tilting the specimen about the eucentric axis of the specimen holder rod, from one extreme of the tilt range to the other. Each projection in real space is equivalent to a central slice in Fourier space and thus, by recording images at successive tilts, the 3D Fourier space of the object is built up slice by slice. It is now possible to fully automate the acquisition process including auto-tracking and auto-focus schemes (Ziese *et al.*, 2002).

In practice, as illustrated in Fig. 1, reconstruction is achieved using a back-projection method. By smearing the original image back into an object space at the angle of the original projection, a 'ray' is generated that will uniquely describe an object in the projection direction. Using a sufficient number of projections, from different angles, the superposition of all of the back-projected 'rays' will return the original object (Crowther *et al.*, 1970; Radermacher, 1992).

Reconstructions by back-projection are always blurred with an enhancement of low frequencies and fine spatial detail reconstructed poorly. This is an effect of the uneven sampling of spatial frequencies in the ensemble of original projections. Assuming an even sampling of Fourier space within each projection, this will result in a proportionately greater sampling density near the centre of Fourier space compared with the periphery. This leads to an under-sampling of the high spatial frequencies of the object and a 'blurred' reconstruction. It is

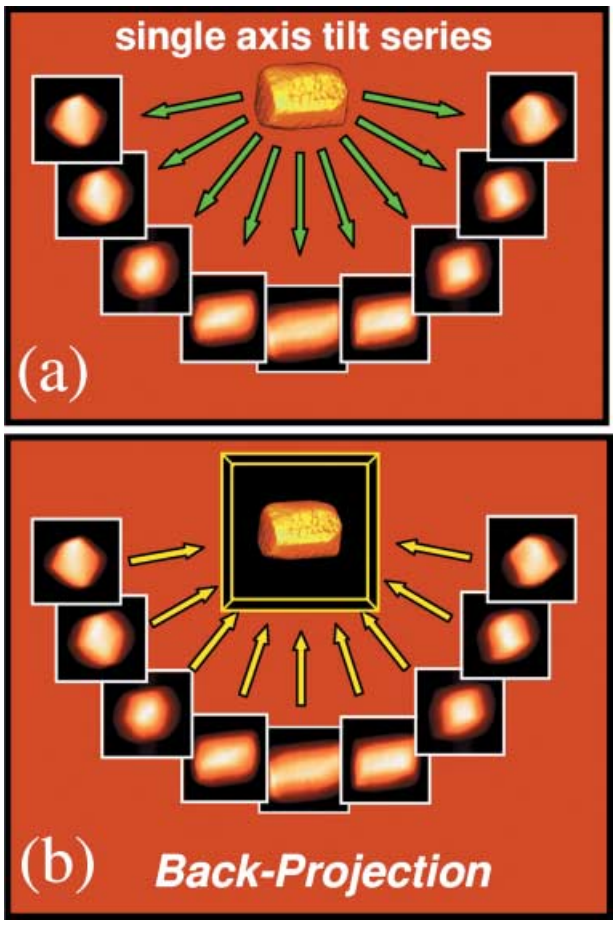

Fig. 1. A schematic diagram of the tomographic reconstruction using the back-projection method. In (a) a series of images are recorded at successive tilts. These images are back-projected in (b) along their original tilt directions into a three-dimensional object space. The overlap of all of the back-projections will define the reconstructed object.

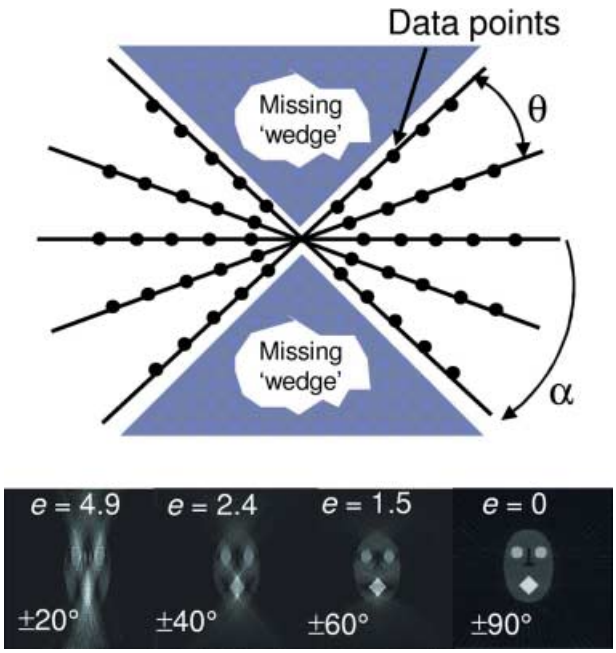

Fig. 2. Representation of Fourier space sampled in a limited tilt series showing the relatively small number of data points at high frequencies, which results in a blurred reconstruction and the missing wedge of information that leads to an elongation, e. The angular sampling is θ and the maximum tilt angle is α.

straightforward to, at least partially, correct for this in Fourier space using a weighting filter (a radially linear function in Fourier space, zero at the centre and a maximum at the edge), an approach known as weighted back-projection.

Reconstructions using the back-projection method will always be 'imperfect' because of the limited sampling and poor signal-to-noise ratio. However, by noting that each projection is a 'perfect' reference, the quality of the reconstruction can be improved. If the (imperfect) reconstruction is reprojected back along the original projection angles, the reprojections, in general, will not be identical to the original projections (images). The difference between them will be characteristic of the deficiency of the reconstruction from the limited dataset. This difference can be back-projected into reconstruction space, generating a 'difference' reconstruction, which can then be used to modify the original reconstruction in order to correct the imperfections in the back-projection. This constrains the reconstruction to agree with the original projections. As the 'difference' is also being back-projected, a single operation will not fully correct the reconstruction and the comparison operation must be repeated iteratively until a 'best' solution is reached. This approach has been used with great success in the tomographic study of a number of materials (e.g. Midgley & Weyland, 2003).

In general, for the single-axis tilt geometry, the spatial resolution of the reconstruction is anisotropic. Parallel to the tilt axis, say the x-axis, the resolution, d_x, is equal to the original resolution of the projections, assuming a perfect tilt series alignment. The resolution in the other perpendicular directions is controlled by the number of projections acquired, N, and the diameter, D, of the volume to be reconstructed (Crowther *et al.*, 1970) and is $d_y = d_z = (\pi D)/N$. In practice, the limited space between the objective lens pole pieces and the finite thickness of the specimen holder limits the tilt range, giving rise to the 'missing wedge' of information (see Fig. 2). This missing information leads to the resolution in the direction parallel to the optic axis, d_z, being degraded further by an 'elongation factor', e_{yz}, so that $d_z = d_y e_{yz}$ which is related to the maximum tilt angle, α (in radians), by $e_{yz} = \sqrt{(\alpha + \sin\alpha\cos\alpha)/(\alpha - \sin\alpha\cos\alpha)}$. Examples are shown in Fig. 2. To maximize the available tilt range, new tomography holders have been introduced with narrower, thinner profiles, which can easily reach ± 70 tilt (an elongation factor of only 1.3), or even higher, without undue shadowing or problems with the pole piece gap.

Scanning transmission electron microscopy HAADF imaging

Any signal used for a tomographic reconstruction must satisfy the projection requirement, which states that the intensity recorded in a projection (image) must be a monotonic function of an object's physical property (Hawkes, 1992). In general, for most (crystalline) specimens in the physical sciences, conventional bright-field imaging will depend strongly upon the diffraction condition of the crystal and this will not have a monotonic relationship with the amount of material through which the beam passes. Therefore, in general bright-field images of crystalline systems cannot be used for tomography because they are not strictly projections. Further, even if the specimen is amorphous or weakly diffracting, the 3D nature of the specimen coupled with the short depth of focus in the TEM ensures that Fresnel contrast will be very apparent [especially if using a field emission gun (FEG) instrument] and this again cannot satisfy the projection requirement. In general, to overcome the problem of Fresnel contrast and diffraction effects, the signals acquired must be predominantly incoherent in nature. Both STEM HAADF (Z-contrast) imaging (Midgley *et al.*, 2001) and energy-filtered TEM (Möbus & Inkson, 2001; Weyland & Midgley, 2003) are, or can be made to be, incoherent in nature and both are chemically sensitive enabling the 3D structure and composition to be mapped simultaneously at high spatial resolution.

An HAADF STEM image is formed by collecting a signal using an annular detector whose inner angle is larger than that of any significant Bragg reflections (Howie, 1979). If the collection angle is large enough, the signal is formed primarily from unscreened elastic and quasi-elastic phonon-scattered electrons. The nature of the scattering and its azimuthal averaging lead to an almost completely incoherent signal, which is sensitive to changes in specimen thickness and atomic number, Z, and approximated to a Z^2 dependence in the high angle limit. Figure 3 shows a comparison between a conventional bright-field image of a multiple quantum well structure, which is dominated by coherent scattering and bend contours, and a STEM HAADF image, in which the quantum wells are much more readily visible.

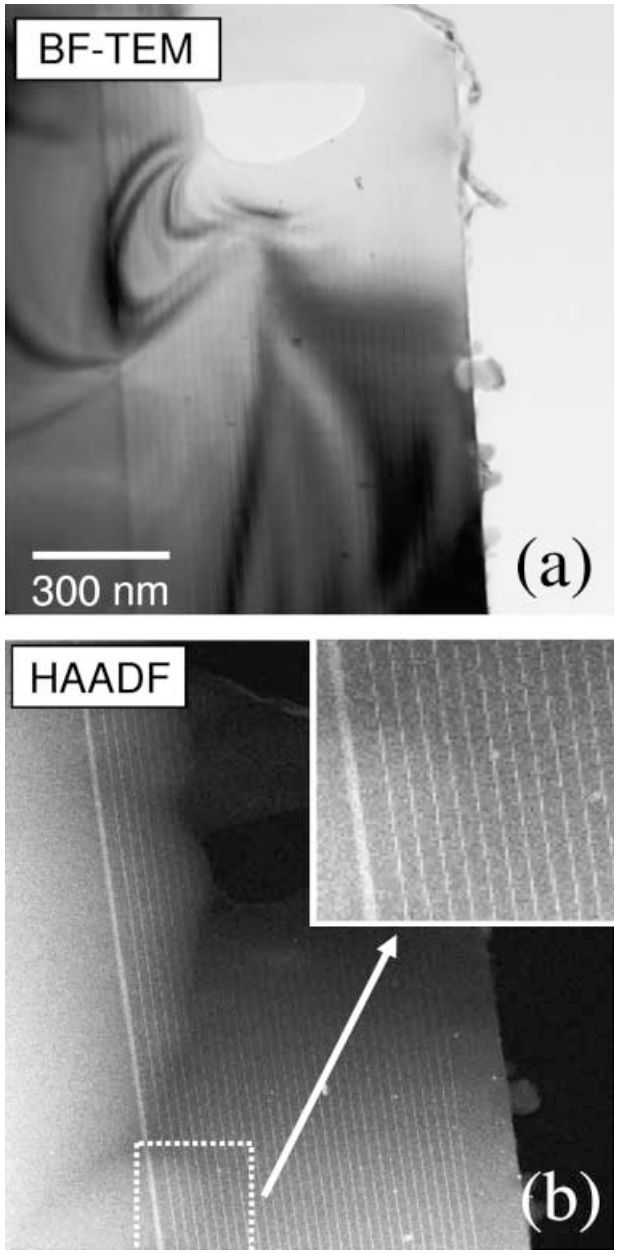

Fig. 3. A comparison of (a) a bright-field (BF) image and (b) a scanning transmission electron microscopy (TEM) HAADF image from an Si/SiGe quantum well structure.

Examples of scanning transmission electron microscopy tomography

The first example of STEM tomography is used to illustrate the resolution achievable with this technique and to illustrate how the 3D distribution of nanometre-sized particles can be determined in a porous support. The specimen is a heterogeneous catalyst composed of $Ru_{10}Pt_2$ bimetallic particles (each with a diameter of about 1 nm) within a mesoporous silica support (MCM-41) whose mesopores are hexagonal in cross-section with a diameter of about 3 nm (Ozkaya *et al.*, 1999). This catalyst has proven to be remarkably successful in hydrogenating *trans, trans*-muconic acid to adipic acid, the former derived from glucose and the latter used to make nylon. Knowledge of the 3D distribution of the metal nanoparticles, and their location at or close to the walls of the internal pores, is key to understanding the factors that govern the activity and selectivity of the nanocatalysts and their change during reaction as a possible result of sintering and coalescence.

Figure 4(a) shows a tomographic reconstruction displayed as a voxel projection of the reconstructed 3D catalyst, viewed parallel to the MCM-41 pore structure. The tomogram was

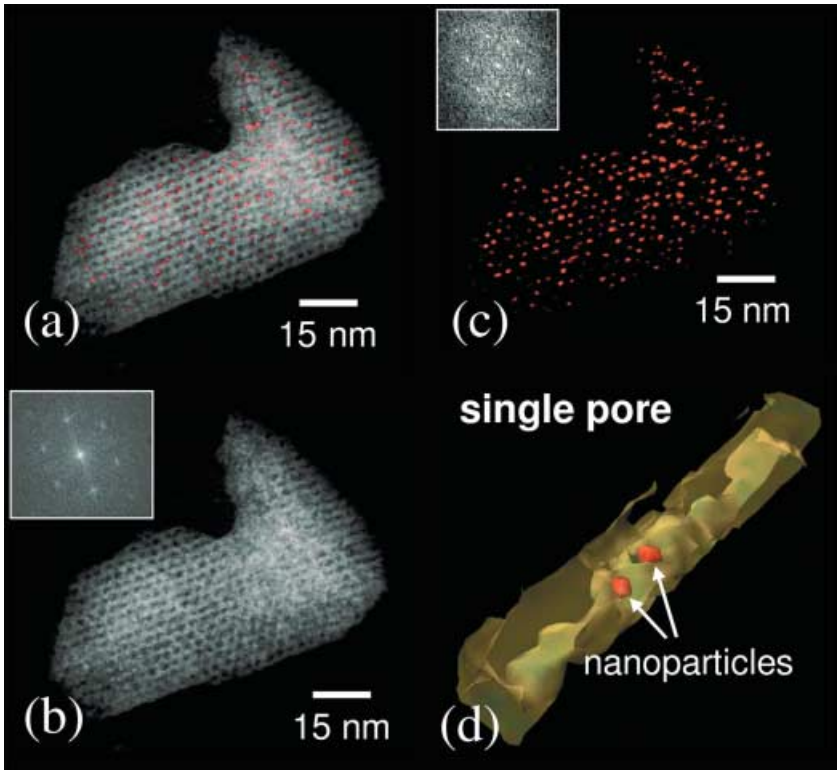

Fig. 4. (a) Voxel projection of a tomographic reconstruction of a heterogeneous catalyst composed of Pt/Ru nanoparticles (red) within an MCM-41 mesoporous silica (white). The two components are separated in (b) and (c); their insets are power spectra revealing the hexagonal symmetry. (d) The position of two nanoparticles within a single mesopore.

constructed from a series of 71 STEM HAADF images taken at 200 kV from +70 to −70 in 2 steps. The nanoparticles are well resolved within the silica framework structure and it is evident that the majority of pores have particles within them. The 3D data set allows a simple segmentation of the data into pores and particles to better reveal the hexagonal arrangement of the pores (Fig. 4b) and the particle distribution (Fig. 4c). Further, it is possible to extract individual pores to determine the number of particles within a pore (Fig. 4d) and, knowing the Pt/Ru mass density and the silica area (from tomogram surface measurements), a catalyst loading can be estimated, i.e. the weight of catalyst per unit surface area (Thomas *et al.*, 2004). Analysis of the reconstruction reveals that the mesoporous structure of the silica has been reconstructed faithfully with little sign of beam damage despite the long acquisition time (~3 h) needed for the series.

Semiconductor quantum dots and similar quantum confinement structures have optical and electronic properties that are dominated by surface and interface states, which may be combined with high strains and have different properties from their bulk counterparts. The morphology of such structures can be the key to understanding their unique properties. Figure 5 shows the tomographic reconstruction of a distribution of (predominantly cubic α-) tin quantum dots buried within a silicon matrix. A representative plan view illustrates the highly facetted surfaces of the buried dots, with the {111} surfaces being the most evident. A cross-sectional view shows how some of the dots (arrowed) appear to be shorter in one direction than the others. This is unlikely to be a reconstruction artefact as the geometry of the tilt series (± 70) would, if anything, lead to a small elongation (not reduction) in that direction.

Figure 6 shows a reconstruction using a series of STEM HAADF images of a multiwall nanotube system in which iron particles, used as a growth catalyst, have been incorporated into the nanotube's internal diameter. The inset shows a phase reconstruction from an electron hologram revealing the stray magnetic field lines associated with one of these iron particles. This relatively low-resolution tomogram illustrates the snake-like structure of the nanotube, and the tensile and compressive surfaces along the tube's length. In addition, it illustrates that high-fidelity reconstructions are possible using STEM HAADF images even from specimens of low atomic number such as carbon.

Figure 7(a) shows a series of STEM HAADF images acquired at different tilts of a CdTe 'tetrapod', a colloidal quantum dot that has grown 'legs' parallel to four equivalent <111> directions in the cubic system. As can be seen from this reconstruction, the legs have been heavily deformed and it appears as though they may have been attracted to the carbon support film perhaps through electrostatic forces. Although all of the legs are visible they are clearly not symmetrically disposed about the central 'core', as would have been expected. This relatively high-resolution reconstruction also reveals the rather bulbous excess growths, particularly at the tetrapod's 'foot'.

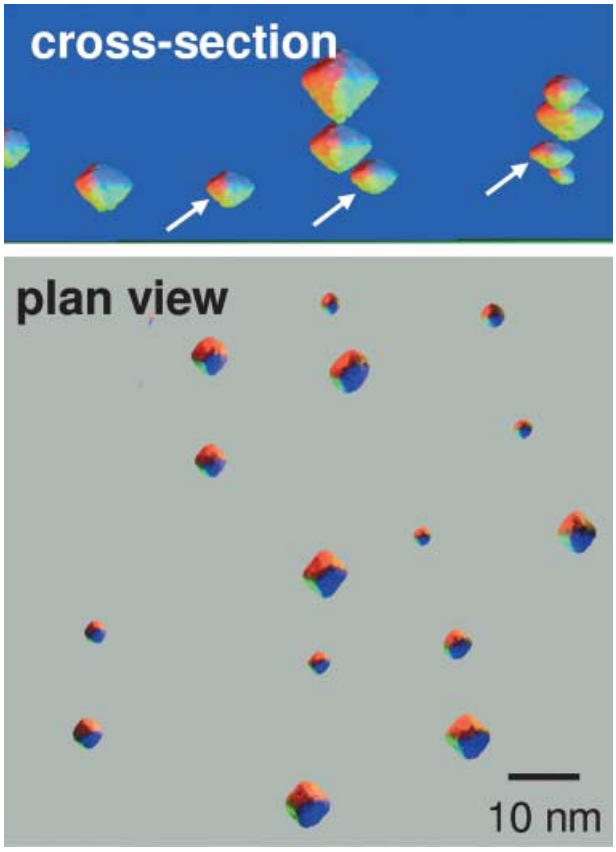

Fig. 5. Cross-sectional and plan view of tin quantum dots buried within a silicon matrix. The dominant {111} facetting of the cubic α-Sn crystals is evident. The arrowed crystals appear rather oblate in form.

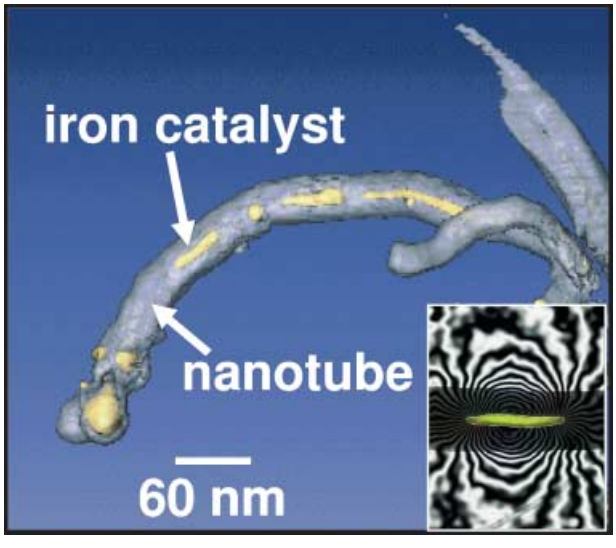

Fig. 6. A surface-rendered reconstruction of a multiwall nanotube in which a number of magnetic iron particles have been encapsulated. The ferromagnetic state of the iron is demonstrated by the holographic phase image in the inset.

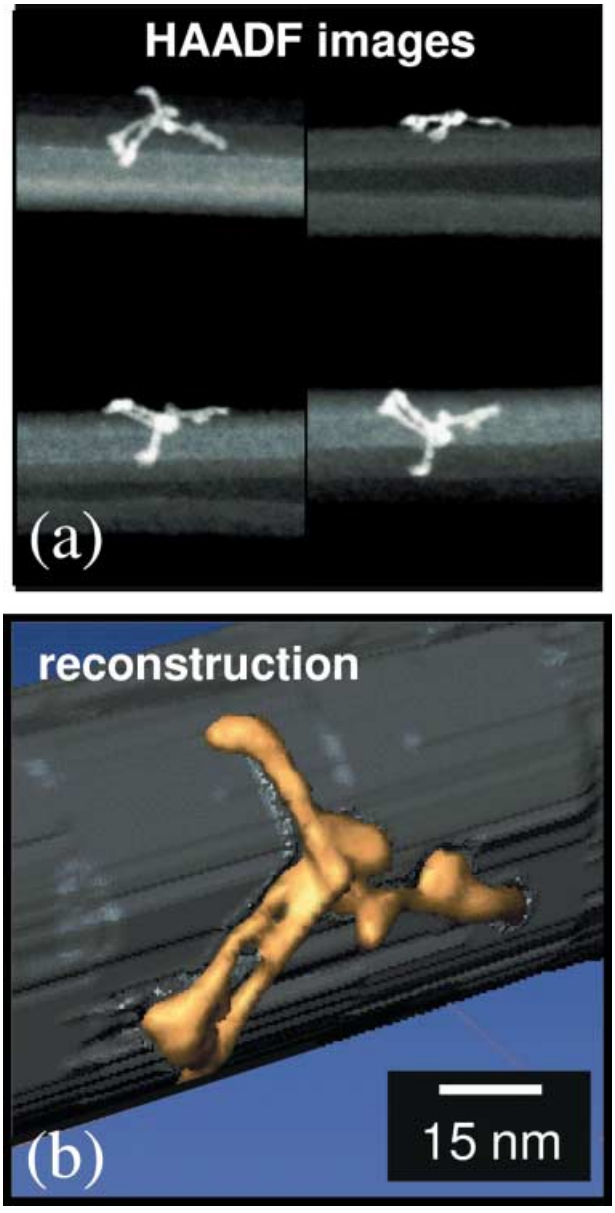

Fig. 7. (a) A tilt series of scanning transmission electron microscopy HAADF images recorded from a CdTe tetrapod. (b) A surface-rendered reconstruction of the tetrapod showing deformation of the leg geometry and an attraction to the carbon support.

Conclusions

The ability to use STEM HAADF images for electron tomographic reconstructions has allowed many specimens to be examined in three dimensions at nanoscale resolution. It has been shown that such tomographic reconstructions can be used to easily differentiate volumes of material with different atomic number. Specimens with low atomic number, and thus low cross-sections for HAADF imaging, can still be reconstructed in three dimensions with STEM tomography. Individual

particles with a diameter of 1 nm can be imaged in three dimensions and low index facets can be revealed from sub-10-nm crystals.

Acknowledgements

The authors wish to thank the Engineering and Physical Sciences Research Council, Royal Society, Royal Commission for the Exhibition of 1851, Isaac Newton Trust and FEI Company for financial support. We thank N. Browning for helpful discussions and for provision of the quantum dot and tetrapod samples. We thank K. Koziol for the provision of the nanotube sample.

References

Banhart, J. (2001) Manufacture, characterization and application of cellular metals and metal foams. *Prog. Mat. Sci*. **46**, 559–632.

Crowther, R.A., de Rosier, D.J. & Klug, A. (1970) The reconstruction of a three-dimensional structure from projections and its application to electron microscopy. *Proc. Roy. Soc. Lond. A*, **317**, 319–340.

Hawkes, P.W. (1992) The electron microscope as a structure projector. *Electron Tomography: Three-Dimensional Imaging with the Transmission Electron Microscope* (ed. by J. Frank), pp. 17–38. Plenum Press, New York.

Hirano, T., Usami, K., Tanaka, Y. & Masuda, C. (1995) In-situ X-ray CT under tensile loading using synchrotron radiation. *J. Mat. Res*. **10**, 381–386.

Howie, A. (1979) Image contrast and localized signal selection techniques. *J. Microsc*. **117**, 11–23.

Marsh, B.J., Mastronarde, D.N., Buttle, K.F., Howell, K.E. & McIntosh, J.R. (2001) Organellar relationships in the Golgi region of the pancreatic beta cell line, HIT-T15, visualized by high resolution electron tomography. *Proc Natl Acad. Sci. U.S.A*. **98**, 2399–2406.

Midgley, P.A. & Weyland, M. (2003) 3D electron microscopy in the physical sciences: the development of Z-contrast and EFTEM tomography. *Ultramicroscopy*, **96**, 413–431.

Midgley, P.A., Weyland, M., Thomas, J.M. & Johnson, B.F.G. (2001) Z-contrast tomography: a technique in three-dimensional nanostructural analysis based on Rutherford scattering. *Chem. Commun*. **18**, 907–908.

Miller, M.K. (2000) *Atom-Probe Tomography: Analysis at the Atomic Level*. Kluwer Academic/Plenum Press, New York.

Möbus, G. & Inkson, B.J. (2001) 3-Dimensional reconstruction of buried nanoparticles by element-sensitive tomography based on inelastically scattered electrons. *Appl. Phys. Lett*. **79**, 1369–1371.

Ozkaya, D., Zhou, W.Z., Thomas, J.M., Midgley, P.A., Keast, V.J. & Hermans, S. (1999) High resolution imaging of nanoparticle bimetallic catalysts supported on mesoporous silica. *Catalysis Lett*. **60**, 113–120.

Radermacher, M. (1992) Weighted back-projection methods. *Electron Tomography: Three-Dimensional Imaging with the Transmission Electron Microscope* (ed. by J. Frank), pp. 91–116. Plenum Press, New York.

Thomas, J.M., Midgley, P.A., Yates, T.J.V., Barnard, J.S., Raja, R., Arslan, I. & Weyland, M. (2004) The chemical application of high-resolution electron tomography. Bright field or dark field? *Angew Chemie Int. Ed*. **43**, 6745–6747.

Weyland, M. & Midgley, P.A. (2003) Extending energy filtered transmission electron microscopy (EFTEM) into three dimensions using electron tomography. *Microsc. Microanal*. **9**, 542–555.

Ziese, U., Janssen, A.H., Murk, J.L., Geerts, W.J.C., Krift, T., Verkleij, A.J. & Koster, A.J. (2002) Automated high-throughput electron tomography by pre-calibration of image shifts. *J. Microsc*. **205**, 187–200.